Model-driven development of durable and scalable thermal energy storage materials for buildings

Shuang Cui [a,b,*], Ravi Anant Kishore [a], Pranvera Kolari [a], Qiye Zheng [c,d,e], Sumanjeet Kaur [c,***], Judith Vidal [a,**], Roderick Jackson [a]

[a] *National Renewable Energy Laboratory, Golden, CO, 80401, United States*
[b] *University of Texas at Dallas, Richardson, TX, 75080, United States*
[c] *Lawrence Berkeley National Laboratory, Berkeley, CA, 94720, United States*
[d] *The Hong Kong University of Science and Technology, Clear water bay, Kowloon, Hong Kong SAR, China*
[e] *University of California at Berkeley, Berkeley, 94720, CA, United States*

ARTICLE INFO

ABSTRACT

The energy impact of integrating phase change materials (PCMs) in buildings for thermal energy storage has been modeled by various whole-building simulation programs, demonstrating that PCM incorporation can reduce energy consumption, provide grid flexibility and resilience, and reduce CO_2 emissions. The models assume that the PCMs are in perfect operating condition and underestimate the impact of actual phase change behavior (e.g., enthalpy curve shape) on thermal load shifting in practical deployment. In this paper, we bridge the gap between theory and practice when evaluating the energy impact of PCMs by using a model-driven approach to develop durable thermal energy storage materials with desired phase change properties. For ease of integration, we fabricate shape-stabilized PCMs (ss-PCMs) by encapsulating solid-liquid polyethylene glycol (PEG) consisting of different molecular weights within mesoporous magnesium oxide (MgO) matrices. Learning from the modeling results, we manipulate phase change properties such as peak melting temperature and temperature glide of PEG-MgO ss-PCMs during the synthesis process to achieve desired properties. As such, the energy density is maximized within the optimum operating temperature range, which is critical to boosting energy efficiency. Compared to a case with no PCM, a layer of PEG-MgO ss-PCM integrated into the wall provides a 50% reduction in the peak load and also exhibits a repeatable phase change behavior for up to 1000 thermal cycles without leakage, showing durability of this material. We also show that this lab-scale synthesis process is easy to be scaled up by 100 times for a demonstration of large-scale industrial production. The synthetic tunability of transition temperature of ss-PCMs also extends their applicability beyond buildings.

1. Introduction

Buildings represent a large portion of the world's energy consumption and associated CO_2 emissions—39% and 40% of the energy consumption and 38% and 36% of the CO_2 emissions in the U.S. and Europe, respectively [1,2]. As such, the development of grid-interactive efficient buildings is essential for energy efficiency. Phase change materials (PCMs) have been proposed for latent thermal energy storage (TES) for grid flexibility and resilience. PCMs can balance the diurnal and nocturnal energy demand by reducing heating/cooling loads and shifting peak loads when integrated into building envelopes [3–6]. Among current solid-liquid, solid-solid, and solid-gas PCMs, solid-liquid PCM has attracted great attention for its appropriate phase transition temperature and high latent heat for building envelopes. However, the inevitable issue with use of solid-liquid PCMs for building envelope applications is the risk of PCM leakage during its melting process [7–9]. To tackle this issue, efforts have been made to prepare shape-stabilized PCMs (ss-PCMs) by impregnating PCMs within a supporting porous material with high surface area and porosity, such as expanded graphite and fumed silica [10–13]. The pore confinement and the mutual interaction between pore surface and PCM molecules through physical

---

Nomenclature

DSC	Differential scanning calorimetry
D_{ED}	Average exudation circle diameter
D_{TD}	Test area diameter
ΔH	Enthalpy (kJ/kg)
MW	Molecular weight
PCM	Phase change material
PEG	Polyethylene glycol
ss-PCMs	Shape-stabilized PCMs
TES	Thermal energy storage
T_t	Transition temperature (°C)
T	Temperature (°C)
q''	Heat flux (W/m^2)

LWR	Long wave-length radiation
Greek Symbols	
Φ	Exudation ratio
ρ	Density (kg/m^3)
C	Specific heat (kJ/kg·K)
k	Thermal conductivity (W/m·K)
α	Solar absorptance
Subscripts	
int	Interior side of the wall
ext	Exterior side of the wall
out	Outdoor condition

---

interactions such as capillary forces, surface tension, and hydrogen bonding can prevent the leakage of PCMs during the melting process but also profoundly affect the physical properties of fluids [14]. Additionally, promoting the interaction between pore surface and PCM molecules, such as increasing the surface area and pore volume, strengthening the capillary force, and creating more hydrogen bonding, promote the shape stability and long-term durability of ss-PCMs.

Typically, to quantify the thermal and energy performance of PCMs embedded in building envelopes, various mathematical PCM models have been developed into prevalent whole-building simulation programs such as EnergyPlus®, TRNSYS, and ESP-r [15]. These types of models calculate building energy consumption based on detailed building and environmental parameters such as building construction details, operation schedules, heating, ventilating, and air conditioning design information, and climate conditions. As such, most modeling studies focus on the building scale or urban scale [16], and assume perfect PCM behavior—for example, a fixed phase transition temperature with a narrow and uniformly distributed enthalpy within the transition temperature range. Only a few researchers considered commercially available PCMs' properties when demonstrating their energy impact on buildings [17–19]. This suggests that the PCMs' intrinsic phase change properties—for instance, actual enthalpy-temperature curve, onset/peak melting temperature, and subcooling—are underestimated in terms of their impacts on building energy efficiency, especially during the material design process, which limits the accuracy of PCM evaluation for implementation in practical applications.

In this study, we propose a model-driven material synthesis approach for ss-PCMs' development in buildings. The goal of the study is to accelerate ss-PCM development for durable TES in building envelopes by considering the detailed phase change properties of PCMs. Among the current solid-liquid PCM compounds, such as organic polyethylene glycols (PEG), paraffin, and fatty acids as well as inorganic hydrated salts [20], we selected PEG as the PCM candidate because it is environmentally benign and exhibits less phase segregation [21]. PEGs with a molecular weight (MW) of 1,000, 800, and 600 g/mol–which are less-studied PCMs for TES for buildings (especially the latter two) —are utilized for fabricating ss-PCMs by fine-tuning the transition temperature suitable for building envelope applications. Mesoporous carriers, e. g., magnesium oxide (MgO), are used for retaining PEG for shape stability, longer lifetime, and enhanced safety due to their high thermal stability, chemical compatibility, high surface area, and low cost. To deliver durable ss-PCMs for practical TES deployment, a physics-based thermal model formulated using COMSOL Multiphysics is used to guide the design and synthesis of PEG-MgO ss-PCMs by predicting theoretical maximum energy performance while considering detailed phase change behavior—for example, enthalpy curve shape. Furthermore, the form stability, fire safety, and long-term durability of

developed ss-PCMs are investigated and we demonstrate a large-scale production method for fire-safe PEG-MgO ss-PCM with long-term form stability over 1000 phase transformation cycles, suitable for TES in building envelopes.

2. Methods

2.1. Materials and materials synthesis

2.1.1. Materials

Reagent grade PEG with a MW of 1000 (PEG1000) and 600 (PEG600), magnesium nitrate hexahydrate (Mg(NO$_3$)$_2$·6H$_2$O), Pluronic F127, and anhydrous ethanol (<0.005% water) were purchased from Sigma Aldrich. Reagent grade PEG with a MW of 800 (PEG800) was purchased from Shandong Baovi Energy Technology Co., Ltd.

2.1.2. Synthesis of mesoporous MgO and PEG-MgO ss-PCMs

Mesoporous MgO was prepared through a combination of evaporation-induced surfactant assembly and magnesium nitrate pyrolysis [22]. The mixture of magnesium nitrate hexahydrate and Pluronic F127 was dissolved in anhydrous ethanol and stirred for 12 h at room temperature. Anhydrous ethanol was then evaporated in the oven for 12 h. Calcination of the Mg-coordinated-F127 precursor was then achieved by increasing the temperature from room temperature to 400 °C and holding for 2 h in the air. PCM (pure PEG or PEG blends) was dissolved in anhydrous ethanol, followed by the addition of MgO to the solution. The mixture was stirred for 4 h at room temperature, after which the ethanol was evaporated at 60 °C in air. The PEG blend (PEG1000/600 or PEG800/600) was prepared by varying ratios of PEG1000, PEG800, and PEG600 and stirred at 50 °C.

2.2. Materials characterization

2.2.1. Morphology and composition

The microstructure of mesoporous MgO and PEG-MgO ss-PCMs was studied using a scanning electron microscope (SEM; Hitachi S–3400 N) and transmission electron microscopy (TEM; Philips CM-30). The chemical compositions of pure PEG, mesoporous MgO, PEG-MgO ss-PCM were further studied via the Fourier Transform Infrared spectroscopy (FT-IR; Thermo Scientific Nicolet 6700) from 525 to 4000 cm^{-1} with a resolution of 0.482 cm^{-1} and thermogravimetric analyses (TA Instruments TGA55) in a high-purity flow of nitrogen, at which the heating rate is 10 °C/min between 20° and 580 °C. Brunauer-Emmett-Teller (BET) surface area measurements were carried out using a specific surface area analyzer (Micromeritics ASAP2020). The mesoporous MgO was evacuated overnight at an estimated 125 °C. Their N$_2$ adsorption and desorption were obtained in liquid N$_2$ isotherms at −196 °C. The pore size distribution and specific surface area were

obtained with density functional theory. All the samples were dried under vacuum at 60 °C overnight to eliminate solvent molecules prior to measurement.

2.2.2. Thermal characterization

Phase change properties including phase transition temperature (T_t) and enthalpy (ΔH) of pure PEG, PEG blends, and PEG-MgO ss-PCMs were studied using a differential scanning calorimetry (DSC; TA Instruments Discovery DSC 2500) under a constant stream of nitrogen (50 ml/min) as flushing gas. Hermetically sealed aluminum crucibles were used for DSC measurements. Data analysis was achieved using TRIOS software. Both operating methods—constant heating rate mode (dynamic) and variable heating rate mode (step, also known as isothermal step or step-scan mode) —were used to characterize the T_t and ΔH of PCMs [23,24]. The dynamic mode DSC measurements were taken as a common pattern with a heating rate of 5 °C/min between −20° and 60 °C, followed by a cooling rate of 5 °C/min to return to −20 °C. The melting and crystallization temperatures were taken as the onset points by drawing a line at the point of maximum slope of the leading edge of the DSC peak and extrapolating the baseline on the same side as the leading edge of the peak. The ΔH was calculated by numerical integration of the area under the peaks. The isothermal step DSC is used to characterize the enthalpy-temperature curve of PCMs. The principle of isothermal step mode DSC measurements was explained in detail in the literature [25,26]. Using a heat-flux DSC in isothermal step mode, the ambiance of PCM (placed inside a hermetic crucible) and reference (an empty crucible) is heated up stepwise in given temperature intervals. The PCM temperature follows the steps with some time delay. When the detected heat flow signal decreases to zero, the next temperature step can follow. The temperature resolution of the acquired data is equal to the step size [27,28]. The heat flow signal of each step was integrated using a linear baseline and the cumulative sum was calculated for the determination of enthalpy curves. The step mode DSC measurements with temperature steps of 1 °C and step times of 10 min from 0° to 50 °C were used here to determine the enthalpy curve of PEG-MgO ss-PCM. Thermal conductivity measurements were taken 20 times using either a transient plane source (Thermtest TPS 2200) or a guarded heat flow meter (TA instruments DTC 300) at room temperature under atmospheric pressure, and the averaged values were used as the samples' thermal conductivity in the thermal modeling.

2.2.3. Form stability characterization

The form stability of PEG-MgO ss-PCMs was studied by leakage tests using the diffusion-oozing circle method [29–31]. In this test, a filter paper was used to check the exudation of PEG from the ss-PCM sample. 3 g of pristine PEG and 3 g of ss-PCM powders were placed in the center of the filter paper respectively, which had a diameter of ~1 cm. The materials were then transferred to a 50 °C oven and heated for at least 24 h. Afterward, the average diameter of the exudation footprint was recorded. The exudation ratio ($\Phi=(D_{ED}-D_{TD})/D_{TD}$) of the ss-PCMs was then quantified as the percent change between the test area diameter (D_{TD}) and the average exudation-circle diameter (D_{ED}). When $\Phi <15\%$, the ss-PCM is stable. Table 1 explains the correlation between Φ and the stability of ss-PCMs [29–31].

Table 1
Exudation ratio scale describing form stability [29–31].

Exudation ratio (Φ)	Stability scale
$\Phi < 10\%$	Very stable
$10\% < \Phi <15\%$	Stable
$15\% < \Phi < 30\%$	Less stable
$30\% < \Phi < 50\%$	Not stable
$50\% < \Phi$	Fail

2.3. Mathematical model and numerical simulation

2.3.1. Wall assembly

A reliably validated numerical model is a fast and relatively cost-effective method of evaluating the performance of different PCMs under various realistic operating conditions. We used a similar numerical model that has been described in our previous publications [32–35]. For brevity, we provide only essential information regarding the numerical model for the purposes of this article. As shown in Fig. 1a, we have considered a lightweight building wall assembly comprising an exterior sheathing, an insulation layer, a PCM layer, and an interior drywall. The material properties of all the components are listed in Table 2. More details about the PCM-relevant thermo-physical properties can be found in the Supplemental Information (Fig. S1 and Table S1). To account for the thermal bridging provided by studs, we have employed a two-dimensional model replicating a portion of the wall geometry as shown in Fig. 1b. Based on our prior analysis, we have considered a thin PCM layer with a thickness of 0.25 in. (0.63 cm). We ensured that the thickness of the PCM-integrated wall remains the same as that of the reference wall with no PCM, by replacing insulation with the PCM layer. Since the thermal conductivity of the PCM is higher than that of the insulation, overall, there is an increase in the thermal conductance of the wall due to PCM inclusion; therefore, increasing PCM thickness beyond a certain value (1.27 cm) has a negative impact on total heat gain [35].

2.3.2. Governing equations and boundary conditions

The heat transfer in a stationary solid medium is described using a thermal diffusion equation, which is mathematically expressed as [36]:

$$\rho C \frac{\partial T}{\partial t} + \nabla \bullet (-k\nabla \mathrm{T}) = 0 \tag{1}$$

where ρ, C, and k are density, specific heat, and thermal conductivity of the medium, respectively, and T is the temperature at the point of measurement.

The material properties of the wall components, except the specific heat of the PCM, are assumed to be constant and temperature independent (Table 2). The specific heat capacity of the PCM was calculated using the enthalpy-temperature curve obtained from DSC.

$$C_{PCM}(T) = \frac{dH(T)}{dT} \tag{2}$$

where C_{PCM} and H represent temperature dependent specific heat and enthalpy of the PCMs. Because specific heat is dependent only on the slope of the enthalpy curve, enthalpy was chosen to be zero at an arbitrary temperature below the phase change.

On the exterior side of the wall, we have considered a heat flux boundary condition (q''_{ext}) comprising solar irradiance, convection losses, and long-wave radiation [37–39]:

$$q''_{ext} = \alpha q''_{solar} + h_{ext}(T_{out} - T_{e,wall}) + q''_{LWR} \tag{3}$$

where α is the solar absorptance, q''_{solar} is the solar irradiance, h_{ext} is the convection coefficient, T_{out} is the outside air temperature, $T_{e,wall}$ is temperature of the exterior surface, and q''_{LWR} is the heat transfer due to long-wave radiation.

On the interior side of the wall, we assign a convection boundary condition that is expressed as:

$$q''_{in} = h_{int}(T_{i,wall} - T_{int}) \tag{4}$$

where h_{int} is the convection coefficient, T_{int} is the interior air temperature, and $T_{i,wall}$ is the temperature of the interior surface of the wall.

We also assign symmetry boundary conditions at the centerline of the wall cavity and the stud that ensures no normal heat flux across a boundary, which is given as [40]:
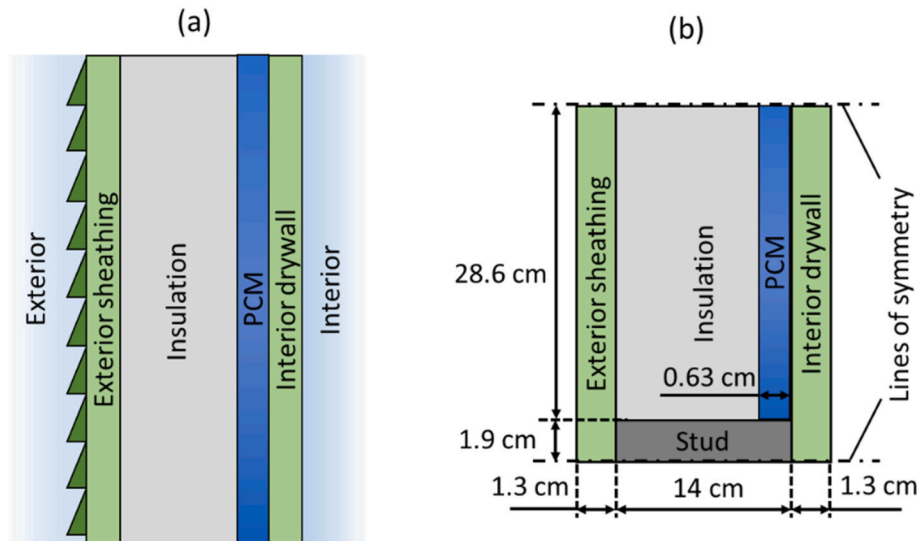
Fig. 1. Wall assembly employed for numerical simulations: (A) Vertical section of the wall comprising PCM layer behind the interior wallboard, (B) Two-dimensional model illustrating wall components and their geometric dimensions.

Table 2
Material properties of different components of the wall assembly [32,33].

Component	Material	Density (kg/m³)	Thermal conductivity (W/m·K)	Specific heat (kJ/kg·K)
Insulation	Expanded polystyrene	24	0.037	1.214
Stud	Wood	577	0.144	1.633
Exterior wallboard	Oriented strand board	640	0.130	1.410
Interior wallboard	Gypsum	550	0.153	1.089
PCM	PEG-MgO	800	0.34	Refer h-T curves

$$q''_\perp = 0 \tag{5}$$

where $q''_\perp$ denotes the heat flux component normal to the boundary.

To study the effect of PCM on the cooling load of a building, we considered Phoenix, Arizona, as the exterior climate. Phoenix is located in International Energy Conservation Code climate zone 2b and represents a hot and dry climate. Typical Meteorological Year 3 data [41] was used to obtain the information needed for exterior climate (q''_{solar}, q''_{LWR}, and T_{out}). The heat transfer coefficients h_{int} and h_{out} on the interior and exterior surfaces were assumed to be 2.5 W/m²·K and 32 W/m·-K, respectively [42,43]. The solar absorptance and the infrared emittance of the exterior surface were assumed to be 0.6 and 0.8, respectively [37–39]. The wall related cooling load (Q_c) due to heat gains through the wall was calculated by time integrating the transient heat gain (q_{gain}) over the given period [32].

$$Q_c(\tau) = \int_{t=0}^{t=\tau} q_{gain}(t) \, dt \tag{6}$$

The average indoor air temperature was taken as 22 °C. To facilitate the load shift, we increase the interior temperature by 1 °C during the peak hours (15:00 to 21:00) and decrease the interior temperature by 1 °C during off-peak hours (0:00 to 6:00). Precooling the building is a recognized technique to allow PCM to charge during off-peak hours, which is later used to decrease the heat gains during peak hours [44]. Please note that temperature variation between 21 °C and 23 °C is within the thermal comfort range of the occupants.

2.3.3. Numerical solution

We employed the commercial finite element code from COMSOL Multiphysics version 5.6 to perform all the simulations. We used the structural quadrilateral mesh with an element count of about 1800 that was obtained after a mesh independence test. The governing equations were solved using a backward differentiation formula, whose order was set with a minimum value of 1 to ensure at least one time step in each subinterval (specified as 1 h) during the time-stepping process. The relative tolerance was prescribed to 0.001 to minimize the error during the computational calculations. Lastly, the model was validated using experimental data available in the published literature as described in our prior publications [32,34]. Please note that while we have used the same wall configuration and the numerical model developed in our prior studies; the goal of this study is to develop new PCMs while the previous papers were targeted to optimize the PCM deployment in the wall.

3. Results and discussion

We present our results in separate subsections as follows:

- Section 3.1 gives a detailed discussion on the model-driven approach of ss-PCM development for building envelope applications. Utilizing physics-based thermal modeling, the phase change properties of PCMs, such as onset/peak melting temperature and temperature glide, are thoroughly investigated for their impact on reducing the peak hours heat gains through the wall in Phoenix, Arizona, United States, which has a hot and dry climate. The modeling delivered guidance on how to tune the phase change behavior of ss-PCMs for maximized energy performance.
- Section 3.2 presents a demonstration of lab-scale fabrication and large-scale production of ss-PCMs with ideal phase change behavior for practical TES deployment. Guided by the thermal modeling, a PEG800/600 blend (40 wt% PEG600)-MgO ss-PCM is developed with optimum peak melting temperature, small temperature glide, and high energy density for maximizing the energy impact in reality. This composition also shows long-term durability with 1000 repeatable phase change transitions and is scaled up by 100 times to demonstrate potential industrial production with minimum variation in phase change behaviors and shape stability.

The schematic of the model-driven development of TES materials for building envelope applications is shown in Fig. 2.
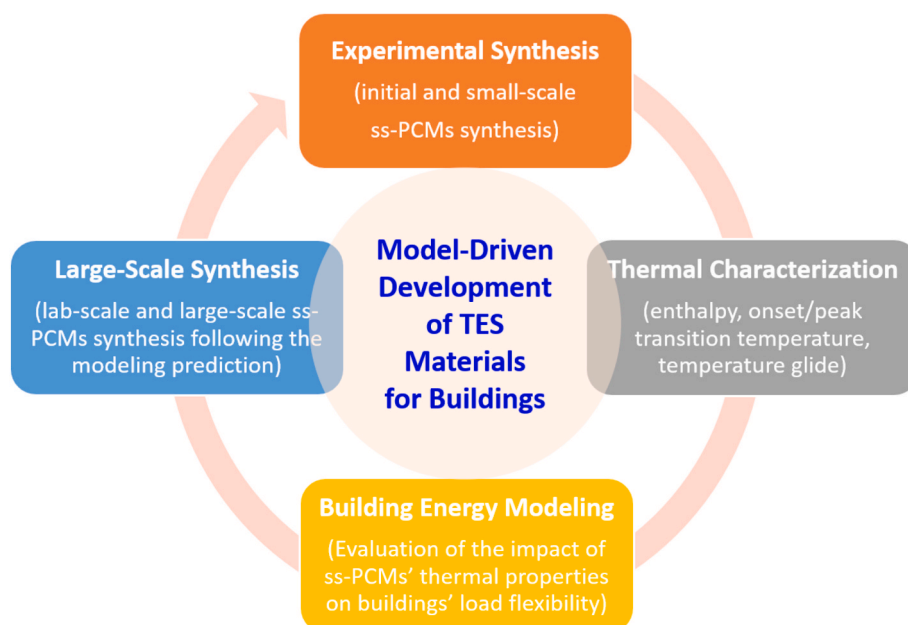
Fig. 2. Schematic of the model-driven approach of ss-PCM development.

3.1. Model-driven prediction and development of PEG-MgO ss-PCMs for maximizing energy performance of PCM-integrated walls

PEG has an onset melting temperature ($T_{m,o}$) range that can be tuned from 14° to 61 °C by varying its MW. Most widely studied PEG has a larger MW ($\geq$1000) for solar energy storage [21,45]. Considering the thermal comfort zone (20.5°–27.5 °C) of human beings, we also selected less-studied PEG600 and PEG800, as well as PEG1000, because their $T_{m,o}$, in the range of 14°–33 °C, is close to the thermal comfort zone. Fig. 3 shows the melting-crystallization curves of (a) Pure PEG and (b) PEG1000/600 blend, which are characterized by dynamic mode DSC. The positive heat flow represents the crystallization process while the negative heat flow represents the melting process. Their corresponding phase change properties are summarized in Table 3. Pure PEG600 has a $T_{m,o}$ of 14.2 °C, which is lower than that of PEG800 (22.6 °C) and PEG1000 (32.3 °C). The $T_{m,o}$ and enthalpy (ΔH) of PEG vary directly proportional to the polymer's average MW. A higher MW PEG results in a higher $T_{m,o}$ and ΔH due to the increase in van der Waals interactions
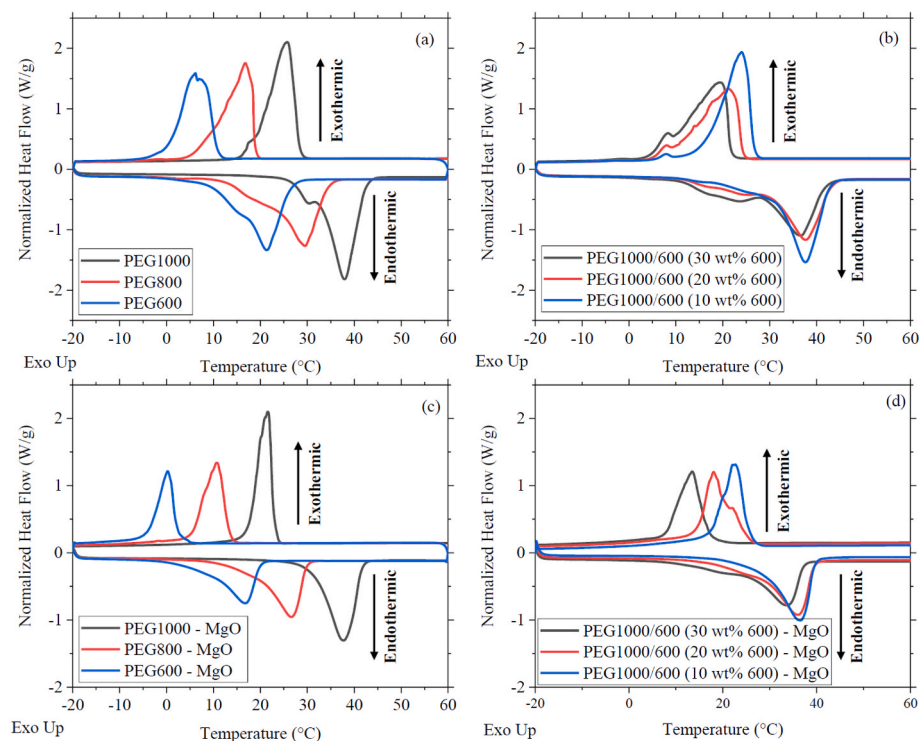

Fig. 3. Typical DSC of (a) pristine PEG with different MWs, (b) PEG1000/600 blends, (c) MgO encapsulated pure PEG, and (d) MgO encapsulated PEG1000/600 blends. The secondary peak in the pristine PEG comes from the dispersity of the polymers, which disappeared after encapsulation with MgO due to the confinement of the matrices.

Table 3
Experimental results for phase change behavior of pure PEG and PEG-MgO ss-PCMs.

Sample	Melting Process			Crystallization Process		
	$T_{m,o}$ (°C)	$T_{m,p}$ (°C)	ΔH_m (J/g)	$T_{c,o}$ (°C)	$T_{c,p}$ (°C)	ΔH_c (J/g)
PEG1000	32.3	37.9	149.6	28.4	25.7	149.1
PEG800	22.6	28.8	144.9	22.3	16.3	139.6
PEG600	14.2	21.3	137.0	10.8	6.2	129.8
PEG1000-MgO	31.5	37.7	100.7	22.9	21.6	93.5
PEG800-MgO	18.3	26.6	86.6	13.4	10.7	76.6
PEG600-MgO	8.1	16.7	68.2	2.2	0.2	58.5
PEG1000/600 (10 wt% 600)	31.4	37.6	161.3	26.3	24.0	155.5
PEG1000/600 (20 wt% 600)	28.7	37.6	159.7	24.1	21.1	153.7
PEG1000/600 (30 wt% 600)	25.8	36.6	150.1	21.6	19.3	144.9
PEG1000/600 (10 wt% 600)-MgO	28.4	36.5	99.7	26.0	22.7	90.9
PEG1000/600 (20 wt% 600)-MgO	26.8	36.0	99.7	22.0	18.0	88.2
PEG1000/600 (30 wt% 600)-MgO	23.8	31.5	92.1	16.9	9.0	84.4

Note: Each composition has been characterized by three individual samples and each sample shows three repeatable DSC cycles. The standard deviation for ΔH is smaller than 0.7 J/g and that for T is smaller than 0.4 °C for all the samples, respectively.

between longer polymer chains [46]. Pure PEG600 and PEG1000 are also mixed and/or mutually dissolved to form a PEG blend by heating for tuning the $T_{m,o}$ within the target thermal comfort zone. When blended with PEG1000, increasing the content of PEG600 depresses the $T_{m,o}$ and broadens both the melting and crystallization peaks. One sharp melting peak and a minor broad undesired peak are observed in both the melting and crystallization curves. The intensity of this minor peak is increased with the enhanced wt.% of PEG600, probably due to the improper mixing of PEG1000 and PEG600.

To fabricate ss-PCMs, we synthesized mesoporous MgO powders and used them to encapsulate pure PEG and PEG blends for form stability. The material synthesis and characterization details are discussed later. Here, we focus on the DSC characterization of PEG-MgO ss-PCMs to study the energy impact of ss-PCM-integrated walls within buildings. Typical DSC curves of mesoporous MgO encapsulated PEG1000, PEG800, and PEG600 ss-PCMs are shown in Fig. 3c. The phase change behavior of the PEG-MgO ss-PCMs is similar to that of the pure PEG. The $T_{m,o}$ of PEG-MgO ss-PCMs are depressed compared to that of pure PEG as reported owing to an increase in the surface energy under nano-confinement [47]. The depressed melting point (T_m) can be estimated from the Gibbs-Thomson equation by Eq. (7), which describes the depression of the T_m of nanoscale spherical particles.

$$T_m(r) = T_m(\infty) + \frac{2T_m(\infty)\sigma_{sl}}{\Delta H_f(\infty)\rho_s r} \tag{7}$$

where $T_m(\infty)$ and ρ_s are the bulk T_m and the solid phase density. $T_m(r)$ is the T_m of crystals with radius r. σ_{sl} is the solid-liquid interface energy.

For the confined system, the radius r and the pore diameter (d) of cylindrical nanopores in a relation of $r = d/2$ [48]. $T_{m,o}$ depression became increasingly pronounced when decreasing the MW of PEGs. A modified Gibbs-Thomson equation where σ_{sl} is replaced by (σ_{sw} - σ_{lw}) [49] indicates smaller interface interactions of the molecules to pore wall (w) for PEG with longer chains. Because the interactions between the chains of PEG1000 tend to be stronger than those among the shorter chains of PEG600, PEG1000 is thus less influenced by the confinement due to the pore wall. Therefore, the ratio of the pore wall-chain of polymer to chain-chain interactions is relatively larger in PEG600 than in PEG1000. This difference in the strength of the interactions between the pore wall and the molecules results in different depressions of the T_t.

The ΔH of the ss-PCMs was also lower than that of pure PEG due to the presence of mesoporous MgO that does not exhibit phase change properties. We use a minimum of 33 wt% MgO to encapsulate PEG for shape stability, which will be discussed in detail later. The melting enthalpy (ΔH_m) of the PEG1000-MgO ss-PCM was reduced by 33% and its crystallization enthalpy (ΔH_c) was reduced by 37%, which aligns well with the wt.% of active PCM in the composite ss-PCM (66 wt%). The slight difference in ΔH between melting and crystallization comes from the crystallinity of PEG [50]. The reduction of ΔH_m for both PEG800-MgO and PEG600-MgO ss-PCMs was greater than expected (40% and 50%, respectively), and as discussed above, could be due to the larger ratio of the pore wall-chain in PEG800 and PEG600 ss-PCMs that enhances the confinement effects.

Based on our prior study, we noted that the optimal transition temperature of an ideal PCM used for buildings' load flexibility in Phoenix is 21°–27 °C [35]. Using this as a guideline, PEG1000/600 blends were encapsulated within MgO matrices to achieve the best performing ss-PCM with a $T_{m,o}$ in this target temperature range. Their phase change behavior and that of the corresponding MgO encapsulated PEG blends were studied by dynamic mode DSC in Fig. 3b and d and summarized in Table 3. Unlike pure PEG-MgO ss-PCM materials, MgO encapsulated PEG1000/600 blends follow a more linear trend upon encapsulation, with the $T_{m,o}$ of each ss-PCM decreasing by 2°–3 °C compared to its corresponding PEG blend. Compared to PEG1000-MgO ss-PCM, the $T_{m,o}$ of PEG1000/600 blend-MgO is further decreased by increasing the wt.% of PEG600. With a 30 wt% of PEG600 incorporation, the $T_{m,o}$ is about 23.8 ± 0.2 °C, which is 7.7 °C lower compared to that of PEG1000-MgO. However, the ΔH_m reduction of each PEG blend after encapsulation with MgO was almost constant (~40%) compared to that of pure PEG-MgO ss-PCM because the enthalpy is dominated by the larger wt.% of PEG1000, which has a higher enthalpy as well as less confinement effect. This also contributes to the disappearance of two undesired distinct melting peaks aforementioned in both the melting and crystallization. As PEG1000/600 (30 wt% 600)-MgO ss-PCM meets the target $T_{m,o}$ of 21°–27 °C, its enthalpy curve is characterized by the isothermal step DSC (Fig. 4a).

To study the impact of onset/peak melting temperature, we obtained the enthalpy curve of the hypothetical material A (shown in Fig. 4b) by shifting the $T_{m,o}$ of PEG1000/600 (30 wt% 600)-MgO towards the left on the x-axis, which has the same temperature glide and maximum ΔH, but a $T_{m,p}$ of 24 °C instead of $T_{m,o}$ of 31.5 °C. Because the temperature glide of hypothetical material A is very large (25 °C) and only a small portion of total enthalpy is utilized for TES, two additional hypothetical materials B and C were developed by shifting the enthalpy curve of PEG1000-MgO ss-PCM and PEG800-MgO ss-PCM to achieve the same $T_{m,p}$ of 24 °C and total enthalpy of 84 J/g, but a smaller temperature glide (13 °C and 18 °C, respectively), compared to PEG1000/600 (30 wt% 600)-MgO ss-PCM. The enthalpy curves of the hypothetical materials B and C are shown in Fig. 4c and d. Using the numerical model, we calculated the energy impact on average heat gains for an indoor temperature of 22 ± 1 °C, with PCM located behind the drywall in a wall assembly at Phoenix that experiences temperature fluctuations between 21 °C and 25 °C, as shown in Fig. 5.

Fig. 5 shows the operating temperature for thermal storage, the energy density of different PCMs under the given temperature range, and their impact on average heat gains through the wall during the off-peak period (0:00 to 6:00), peak period (15:00 to 21:00), and mid-peak period (remaining hours) of a day in a cooling season. The baseline case represents a wall assembly containing no PCM. As shown in Fig. 5a, the PCM layers in the wall experience temperature variations between ~21 °C and 25 °C during the entire cooling season (May–Oct.) in Phoenix. Under these conditions, PEG1000/600 (30 wt% 600)-MgO ss-PCM provides a 27% reduction in peak load, whereas hypothetical materials A, B, and C respectively provide 48%, 60%, and 54% reductions in peak loads (5b). It is interesting to note that while the heat gains during the peak period have decreased, the heat gains during the
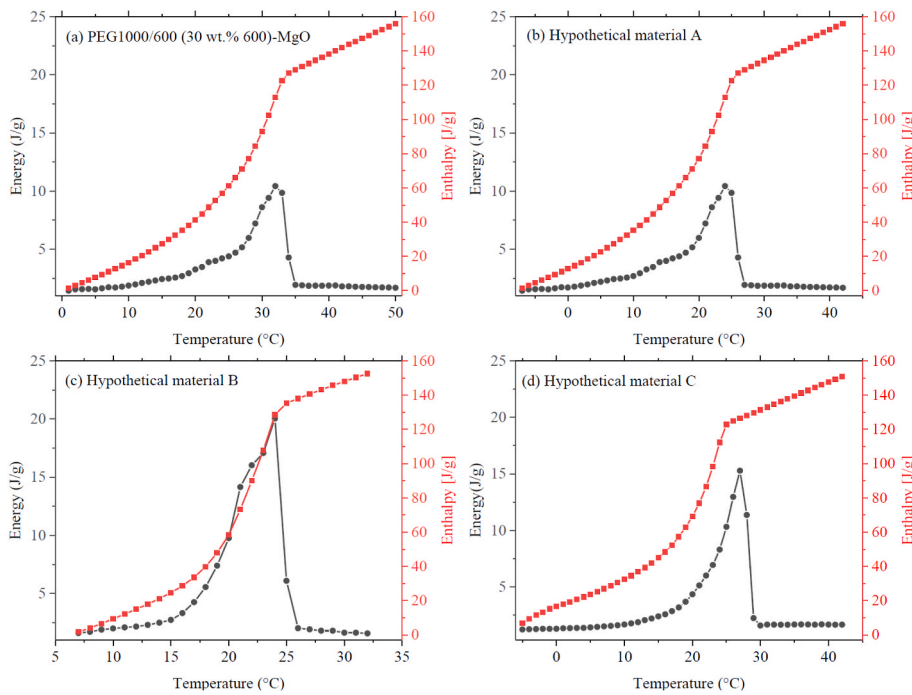
Fig. 4. Enthalpy curves of (a) PEG1000/600 (30 wt% 600)-MgO ss-PCM and (b–d) hypothetical ss-PCMs A-C. The enthalpy curve of PEG1000/600 (30 wt% 600)-MgO ss-PCM was obtained using a heat-flux DSC in isothermal step-mode. The heat flow signal of each temperature step (1 °C in this study) was integrated using a linear baseline and the cumulative sum was calculated for the determination of enthalpy curves. The enthalpy curves hypothetical materials B, C, and D were developed by shifting the enthalpy curves of ss-PCMs with different PEGs.
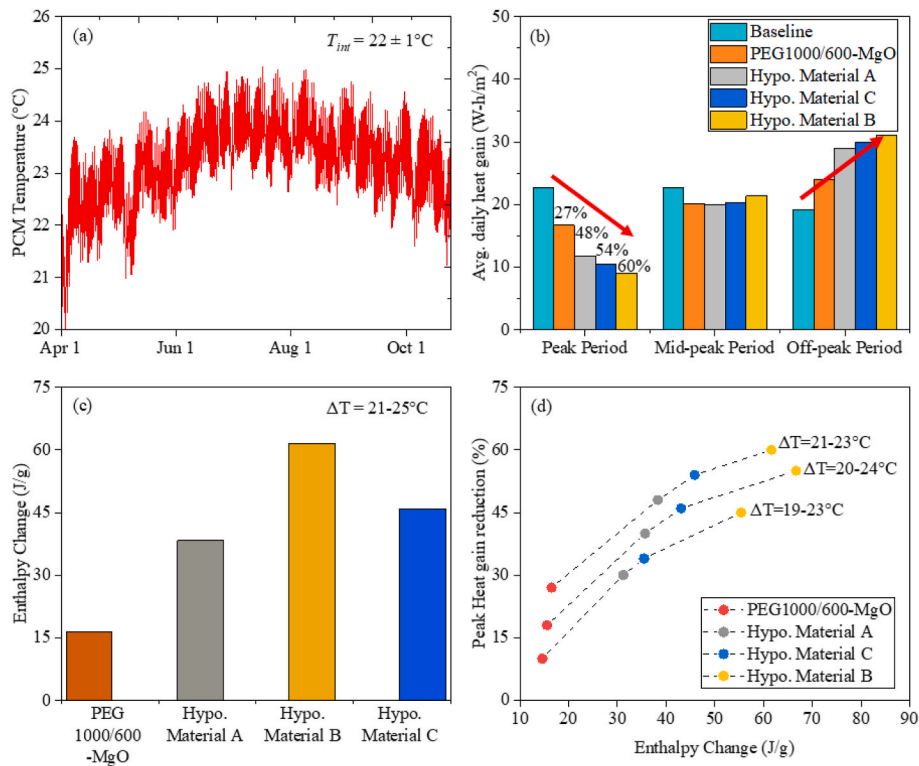
Fig. 5. Model results: (a) Temperature variations experienced by a PCM layer located behind the drywall in a wall assembly in Phoenix during cooling season; (b) Impact of different PCMs in shifting the thermal load from peak to off-peak hours; (c) Enthalpy change of different PCMs under the operating temperature zone; (d) Peak heat gain reduction by various PCMs under different temperature ranges.

off-peak period have increased, implying a shift in the thermal loads from peak to off-peak hours. Fig. 5c shows the enthalpy change of different PCMs in the temperature range of 21°–25 °C (operation temperature zone of PCMs set in the model). Note that while the total enthalpy change of all the PCMs is nearly the same (~160 J/g), the useful enthalpy change for the given temperature is highest for the

hypothetical material B (62 J/g), followed by material C (46 J/g), material A (38 J/g), and lastly PEG1000/600 (30 wt% 600)-MgO (16 J/g). Consequently, the hypothetical material B exhibits the highest impact in shifting the peak thermal load, followed by material C and material A. Fig. 5d shows the performance of different materials when the operating temperature in the model is altered as 19°–23 °C for an interior

temperature of 20 ± 1 °C, 20°–24 °C for an interior temperature of 21 ± 1 °C, and 21°–25 °C for an indoor temperature of 22 ± 1 °C. Interestingly, in all these cases, the order of the materials follows the same trend as the enthalpy change under the given temperature range. Our modeling result thus demonstrates the hypothesis that a PCM with $T_{m,p}$ close to the maximum operating temperature and the highest enthalpy change under the operating temperature range provides maximum TES benefits and thus load flexibility in buildings. This key finding will be utilized to guide the lab-scale material synthesis.

3.2. Modeling guided lab-scale PEG-MgO ss-PCM synthesis and characterization

Guided by the modeling, we aim to synthesize ss-PCMs with a relatively sharp transition peak (small temperature glide) and optimum $T_{m,p}$ just below 25 °C by encapsulating PEG800/600 blends within mesoporous MgO. As shown in Table 4, the $T_{m,p}$ of the PEG800/600 blend can be suppressed by as much as 5.7 °C when increasing the wt.% of PEG600. However, mixing PEG600 with PEG800 has less effect on the temperature glide compared to mixing PEG600 with PEG1000. Compared to PEG1000/600 blends, the secondary phase change peak is less pronounced in PEG800/600 blends (Fig. 6a), which might result from the greater similarity in the MW distribution of PEG800 and PEG600. This also results in a sharper transition peak in PEG800/600 blend-MgO ss-PCMs when the incorporation of PEG600 is less than 40 wt% (Fig. 6b). When further enhancing the wt.% of PEG600 to 50 and 60 wt%, the transition shoulder of PEG800/600 blend-MgO ss-PCM becomes broader like that of PEG600-MgO ss-PCM. The $T_{m,p}$ of PEG800/600 blend decreases linearly after encapsulation when the wt.% of PEG600 is less than 40% and suddenly drops when above 50 wt%. Compared to PEG1000/600 blend-MgO ss-PCM, the ΔH_m of PEG800/PEG600 blend-MgO ss-PCM is depressed more (40–50 wt%) due to the stronger micro-encapsulation confinement of PEG with lower MW as discussed previously.

Table 4
Experimental results for phase change behavior of PEG800/600 blend and PEG800/600-MgO ss-PCMs.

Sample	Melting Process			Crystallization Process		
	$T_{m,o}$ (°C)	$T_{m,p}$ (°C)	ΔH_m (J/g)	$T_{c,o}$ (°C)	$T_{c,p}$ (°C)	ΔH_c (J/g)
PEG800/600 (10 wt % 600)	20.9	29.6	146.6	18.3	15.8	140.5
PEG800/600 (20 wt % 600)	18.9	28.5	146.4	17.5	14.9	139.1
PEG800/600 (30 wt % 600)	17.9	28.1	132.2	12.4	10.5	126.9
PEG800/600 (40 wt % 600)	15.8	27.8	140.4	16.1	12.4	134.3
PEG800/600 (50 wt % 600)	14.3	24.8	138.0	14.2	11.8	132.0
PEG800/600 (60 wt % 600)	14.5	23.9	137.7	13.8	10.6	131.9
PEG800/600 (10 wt % 600)-MgO	17.2	27.5	84.8	24.0	19.3	78.4
PEG800/600 (20 wt % 600)-MgO	15.7	26.9	82.1	20.2	17.4	76.8
PEG800/600 (30 wt % 600)-MgO	15.0	26.7	81.9	16.7	12.2	76.2
PEG800/600 (40 wt % 600)-MgO	13.2	23.4	79.4	13.3	11.0	70.4
PEG800/600 (50 wt % 600)-MgO	8.5	20.1	70.9	7.2	4.1	62.4
PEG800/600 (60 wt % 600)-MgO	7.3	18.9	73.5	7.1	3.2	62.8

Note: Each composition has been characterized by three individual samples and each sample shows three repeatable DSC cycles. The standard deviation for ΔH is smaller than 0.7 J/g and that for T is smaller than 0.4 °C for all the samples, respectively.

3.2.1. Energy impact of PEG800/600 blend-MgO ss-PCMs

To study the impact of lab-synthesized ss-PCM on load flexibility in buildings, the enthalpy curve of PEG800/600 blend (40 wt% 600)-MgO ss-PCM was obtained by step-mode DSC (Fig. 6c) and applied to the building modeling. Fig. 6d compares the performance of lab-synthesized ss-PCM versus the hypothetical material B. Compared to the baseline, lab-synthesized ss-PCM provides a 50% reduction in the peak load, compared to a 60% reduction by the targeted hypothetical material. While the performance of the actual material is slightly poorer than expected due to lower enthalpy change in the range of 21°–25 °C, this study demonstrates that the modeling-guided material synthesis approach can help researchers to achieve the optimal material design for a given climate to maximize TES benefits in buildings.

3.2.2. Microstructure of mesoporous MgO and PEG800/600 blend-MgO ss-PCMs

The morphologies and microstructures of as-synthesized mesoporous MgO after heat treatment were examined by SEM and TEM, shown in Fig. 7. The surfaces of the MgO powders were analyzed and found to exhibit considerable surface roughness. The SEM image reveals a 3D large-scale sponge-like porous structure with many macro-sized pores and voids, which can be easily infiltrated by PEG for PCM impregnation (Fig. 7a). Ultra-fine particles with large specific surface areas usually readily agglomerate to form larger particles due to random interaction between the nanoparticles during heat treatment. The EDX spectrum shows that the mesoporous MgO contains only Mg, O, and a small peak of C, which is present in the carbon tape used for sample preparation for the SEM (Fig. 7c). The EDX mapping indicates that all these elements are homogeneously distributed. The TEM image further confirms that the "sponge" consisted of agglomerated nanoparticles with sizes from 10 to 20 nm (Fig. 7e). The selected area electron diffraction (SAED) pattern (see the inset in Fig. 7e) comprises discontinuous rings, which indicates that the sample consists of polycrystals. A sharp N_2 adsorption-desorption peak of MgO was observed in the high P/P_0 range (Fig. S2). The shape of the isotherms suggests an overall type H3 hysteresis loop indicative of the presence of mesopores, which is excellent for PCM encapsulation [51,52]. If the porous matrix has very small pores, the crystalline behavior of PCMs will be altered and confined, which may not be able to relax to its lowest energy state, thus reducing the latent heat enthalpy [53]. Very large pores cannot confine the liquid PCM within the matrix for form stability. BET analysis also reveals the large surface area of the synthesized porous MgO is 227 m^2/g. The MgO sample shows a Barrett-Joyner-Halenda (BJH) adsorption average pore diameter of 18.5 nm and BJH adsorption cumulative pore volume of 0.73 cm^3/g. The high BET surface area and large total pore volume also confirm that the MgO has a mesoporous structure, which can serve as a good support matrix for ss-PCM preparation and enhance the thermal dependability of PEG-MgO ss-PCM during the melting and freezing cycles.

The PEG-MgO ss-PCMs were prepared by impregnating pure PEG or PEG blends with different MWs into the mesoporous MgO matrix. Fig. 7b reveals the microstructure of the PEG800/600 blend (40 wt% 600)-MgO ss-PCM with a compact and flat surface, which demonstrates the previous porous texture in sponge-like MgO is filled with PEG. These results indicate that the porous structure of the MgO matrix can accommodate a large quantity of PEG to form an efficient shape-stabilized PCM. The PEG incorporation might result from capillary forces and surface tension. The interactions between PEG and the supporting MgO matrix were characterized by Fourier Transform Infrared spectroscopy (FTIR) spectroscopy at room temperature. Fig. 8 shows the FTIR spectra of (a) MgO, (b) PEG800/600 blend (40 wt% 600), and (c) PEG800/600 blend (40 wt% 600)-MgO ss-PCM sample. For the MgO sample, the peak at 3335 cm^{-1} is attributed to the stretching vibration of surface-bound –O–H. It is well known that MgO surfaces readily absorb H_2O and CO_2 molecules when exposed to the atmosphere [54]. The peak at 1428 cm^{-1} is assigned to the asymmetrical and symmetrical stretching vibrations of carboxylate
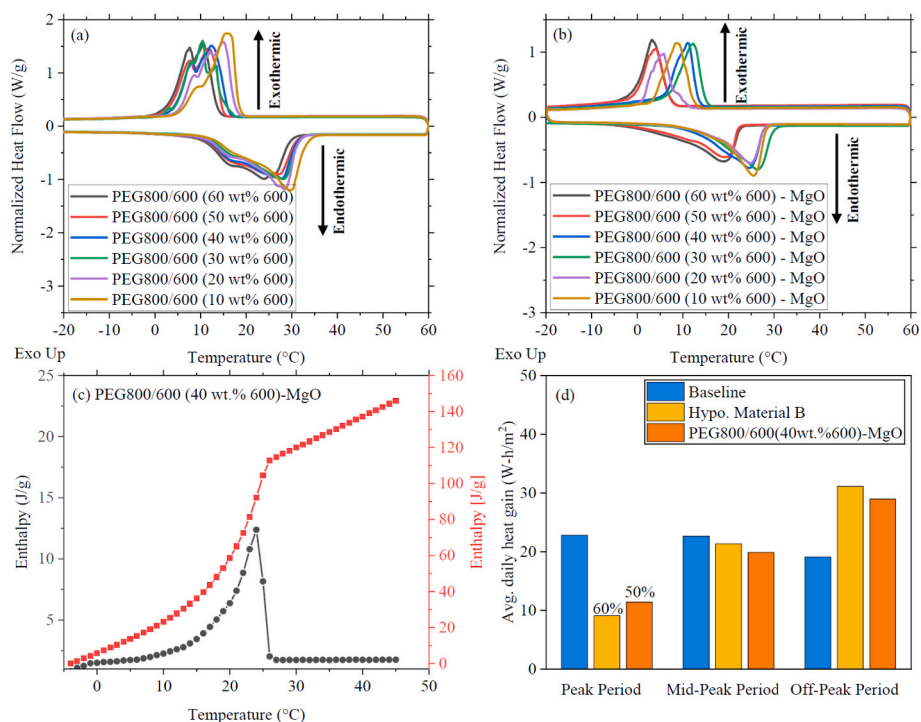
Fig. 6. DSC of (a) PEG800/600 blends and (b) MgO encapsulated PEG800/600 blends; (c) enthalpy curve of PEG800/600 blend (40 wt% 600)-MgO ss-PCM and (d) Load shifting of PEG800/600 blend (40 wt% 600)-MgO ss-PCM.
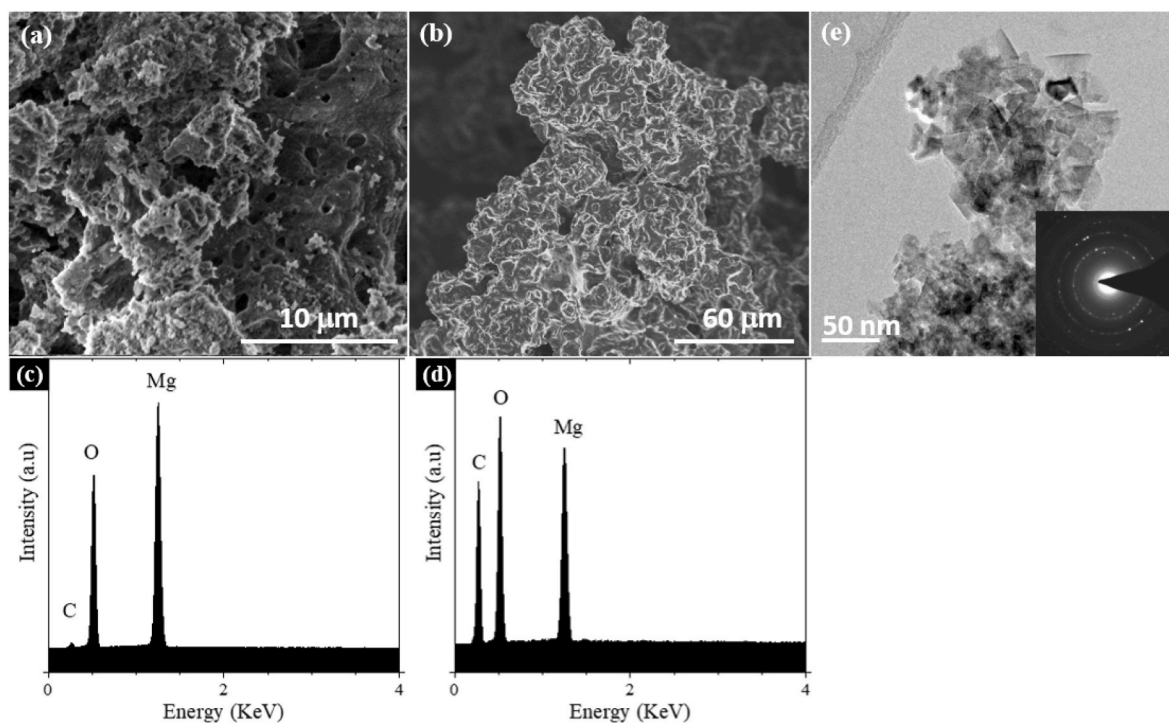

Fig. 7. SEM images of (a) as-synthesized mesoporous MgO and (b) PEG800/600 blend (40 wt% 600)-MgO ss-PCMs; EDX spectra of (c) as-synthesized mesoporous MgO and (d) PEG800/600 blend (40 wt% 600)-MgO ss-PCMs; (e) TEM images of as-synthesized mesoporous MgO.

(O–C═O). For the PEG sample, the peaks at 1465 and 1344 cm^{-1} are due to C–H bending vibrations [55]. The C–O and C–O–H stretching vibrations produce peaks at 1282 and 1241 cm^{-1}, respectively. The peak at 1097 cm^{-1} is due to the stretching vibration of C–O–C. The strong peaks at 2864 and 944 cm^{-1} result from the stretching vibrations of the functional group of –CH$_2$. These absorption peaks can also be observed

in the spectra of PEG-MgO ss-PCM. The absence of any new absorption bands, though, indicates that no chemical bonds are being formed between PEG and MgO. However, the frequency of some absorption bands has shifted slightly, which could mean that hydrogen bonds are formed between bridging oxygen atoms of MgO and the end-hydroxyl group of PEG. This physical interaction would help prevent the leakage of the
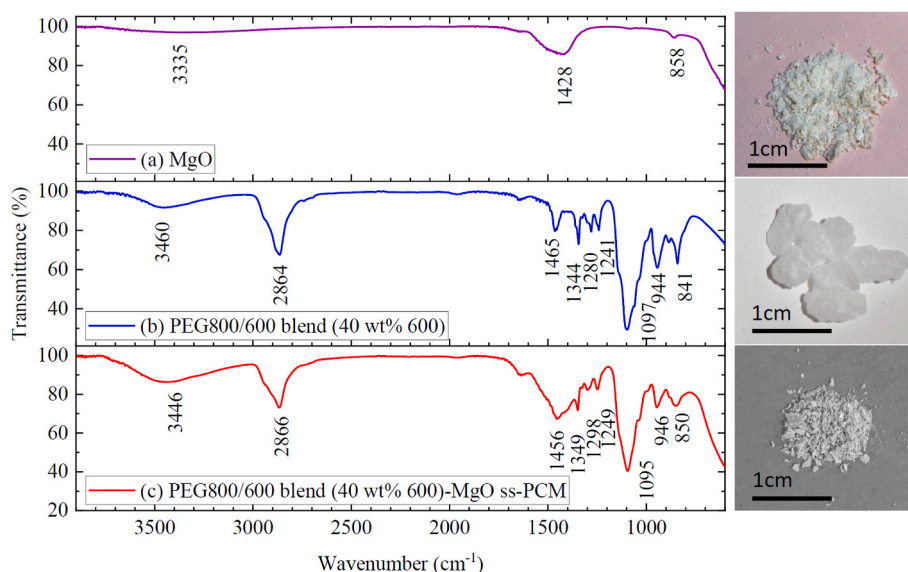
Fig. 8. FTIR spectra of (a) MgO, (b) PEG800/600 blend (40 wt% 600), and (c) PEG800/600 blend (40 wt% 600)-MgO ss-PCM.

molten PEG from the porous MgO matrices.

3.2.3. Stability and durability of PEG800/600 blend-MgO ss-PCM

3.2.3.1. Influence of PEG-loading ratio on form stability. The PEG-loading ratio of PEG-MgO ss-PCM for form stability was determined by the diffusion-oozing circle method. To maximize the thermal load shifting potential of PEG-MgO ss-PCMs in building envelopes, a higher energy density is required. This can be achieved by maximizing the amount of active PCMs, thus minimizing the corresponding portion of inactive supporting mesoporous MgO. One PEG800/600 blend (40 wt% 600) and three mesoporous MgO encapsulated PEG600, PEG800, and PEG800/600 blends (40 wt% 600) with different wt.% (67, 75, and 83) were placed in an oven at 50 °C for 24 h. As shown in Fig. 9, the PEG800/600 blend without MgO encapsulation melted completely after 20 min of heat exposure while the PEG-MgO ss-PCM retained its original solid form during the entire 24 h of treatment with a PEG loading of 67 wt%. Leakage was not evident in any of the samples with the filter paper underneath the ss-PCMs, which showed no footprint signs of leakage (Φ = 0) and mass difference less than 1 wt% (Table 5). The diffusion-oozing result confirms that the porous MgO provides mechanical strength for the composite and prevents the leakage of the molten PEG in the phase transformation process. As increasing the wt.% of PEG loading to 75 wt %, mesoporous MgO fails to keep the form stability with a pronounced footprint of PEG leakage on the filter paper. The exudation ratio Φ is

Table 5
Diffusion-exudation circle test of PEG-MgO ss-PCM.

PCM	PEG (wt. %)	MgO (wt. %)	D_{ED} (mm)	D_{TD} (mm)	Φ (%)
PEG800	67	33	10.2	10.2	0
PEG800	75	25	14.8	10.4	42.3
PEG800/600 blend	67	33	10.1	10.1	0
PEG800/600 blend	75	25	14.8	10.1	46.5
PEG600	67	33	10.1	10.1	0
PEG600	75	25	9.7	24.2	149.5

Note: Each composition has been characterized by three individual samples and each sample shows three repeatable DSC cycles. The standard deviation for ΔH is smaller than 0.7 J/g and that for T is smaller than 0.4 °C for all the samples, respectively.

larger than 15% for all the PEG-MgO ss-PCMs. PEG-MgO ss-PCMs with 83 wt% PEG loading were also prepared but found to sustain insufficient MgO support and high leakage. Although increasing wt.% of PEG loading results in an enhanced ΔH of ss-PCMs, a minimum mass ratio of 33 wt% MgO is necessary to properly encapsulate and contain the PCM for form stability while melting.

3.2.3.2. Thermal stability and long-term durability of PEG-MgO ss-PCMs.
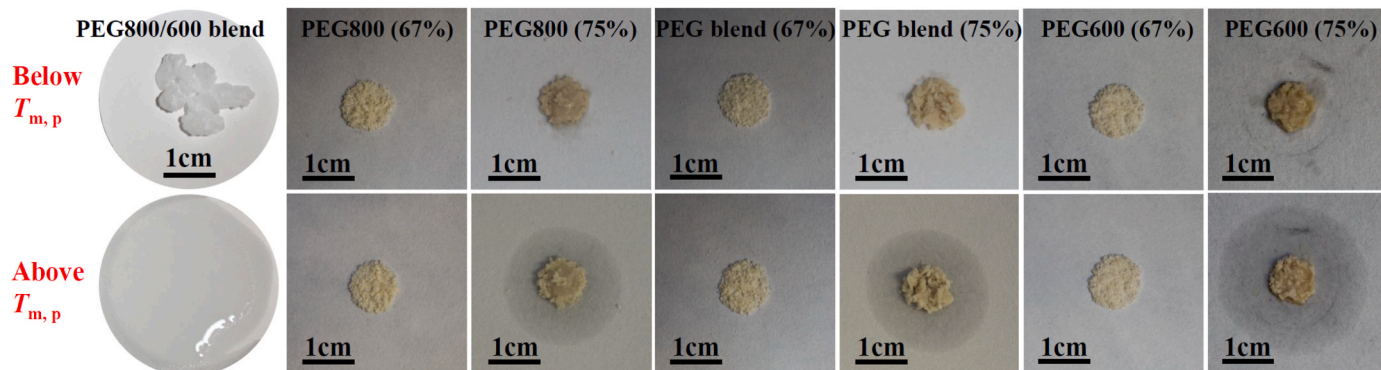

Fig. 9. Photographs of PEG600-MgO and PEG800-MgO ss-PCMs before (top row) and after (bottom row) heat treatment at 50 °C for 24 h. Fraction in parenthesis refers to wt.% of PEG loading.

The thermal stability and actual PEG impregnation ratio of PEG-MgO ss-PCM were determined by TGA measurements as shown in Fig. 10a. The weight loss of pure mesoporous MgO is ~12 wt% up to 580 °C due to the removal of absorbed water and the hydroxyls. Pure PEG800 and PEG600 start to be removed at about 250 °C. The abrupt melting started at 300 °C and a 100% total weight loss percentage was achieved at 400 °C. The weight loss corresponds to the pyrolysis of the PEG functional groups. For the PEG-MgO ss-PCM, the weight loss can be attributed to the removal of PEG molecules from the ss-PCM as well as the absorbed water and the hydroxyls from MgO matrices. The removal temperature of PEG800 from the ss-PCM is similar to that of pure PEG800, suggesting physical interactions between PEG800 and MgO matrices. In comparison, PEG600-MgO ss-PCM has less thermal stability with a lower decomposition temperature. However, the total weight loss percentage of both PEG600-MgO and PEG800-MgO ss-PCMs is the same: ~63% up to 580 °C. The impregnation ratio of PEG (M) in PEG-MgO ss-PCM can be calculated according to the residual weight percentage of the ss-PCM (W) and pure MgO (n), by using the following Eq. (8) [56]. Therefore, the PEG impregnation ratio of PEG600-MgO, PEG800-MgO, and PEG800/600 blend (40 wt% 600)-MgO ss-PCM is ~58%.

$$(1 - M) \times n = W \tag{8}$$

To assess the total weight related energy storage capacity of PEG-MgO ss-PCM, the apparent thermal storage efficiency ($\eta_{apparent}$) of the ss-PCM is calculated using Eq. (9) to be ~60% for PEG800-MgO ss-PCM and ~50% for PEG600-MgO ss-PCM, indicating that almost all PEG molecule chains could effectively store and release heat through a phase transition in PEG800-MgO ss-PCM. However, PEG600-MgO ss-PCM suppresses the enthalpy more due to greater interaction of PEG600 with the walls of MgO matrices as discussed earlier.

$$\eta_{apparent} = \frac{\Delta H_{ss-PCM}}{\Delta H_{PEG}} \times 100\% \tag{9}$$

The decomposition temperature of PEG800/600 blend-MgO ss-PCM is between that of PEG600-MgO and PEG800-MgO ss-PCM. The $\eta_{apparent}$ of PEG800/600 blend-MgO ss-PCM is 57% and also falls between that of PEG600-MgO and PEG800-MgO ss-PCM. The slightly lower $\eta_{apparent}$ of PEG800/600 blend-MgO ss-PCM indicates that not all the impregnated PEG800/600 (64%) contributes to the phase transition, suggesting stronger mutual interaction between PEG600 and MgO matrices.

The long-term durability of PEG-MgO ss-PCM was further assessed using a thermal cycling test with a dynamic mode DSC. Fig. 10b shows the thermal behavior of PEG800/600 blend (40 wt% 600)-MgO ss-PCM at increments of 100 cycles up to 1000 cycles. PEG-MgO ss-PCM shows great thermal reliability with little to no change in T_t and ΔH, demonstrating that mesoporous MgO matrices enhance the thermal stability of the PCM. These results illustrate the feasibility of the PEG-MgO ss-PCM composites for practical applications, considering that thermal cycling in the test encompasses the entire real-world thermal cycling range and

beyond. Additionally, the fire safety properties of PEG-MgO ss-PCM were evaluated with the designed candle test (Fig. S2 and videos in the Supplemental Information) [57], which shows great promise for practical TES in building envelopes. The thermal conductivity of PEG800/600 blend-MgO ss-PCM pressed under 520 PSI is also characterized at room temperature, which is 0.34 W/m·K, slightly higher than that of PEG800/600 blend (0.22 W/m·K) although the PEG blend in both of these samples is in a molten state (Table S1) [58]. This improvement in the thermal conductivity of PCMs in a molten state can potentially increase efficiency due to fast charging/discharging.

3.2.4. 100X scale-up production of PEG-MgO ss-PCM

The synthesis of PEG-MgO ss-PCMs was scaled up in the lab by 100 times to demonstrate its potential in large-scale industrial production and ease of implementation within buildings for practical TES deployment. The scale-up synthesis includes two steps: (1) MgO scale-up synthesis and (2) PEG-MgO ss-PCMs scale-up synthesis. Compared to the small-scale synthesis, the impregnation of PEG into MgO matrices at room temperature takes longer (6x increase) for homogeneous mixing and the ethanol solvent amount is reduced by 4 times for a shorter drying process. To make industrial production more cost effective, the ethanol involved can be potentially replaced with water as well. Fig. 11a shows the phase change behavior of large-scale synthesized PEG800/600 blend (40 wt% 600)-MgO ss-PCMs, indicating no variability in both T_t and ΔH among four samples taken at random. The insert photo in Fig. 11a also reveals a uniform sample apparency. Moreover, the large-scale synthesized samples show similar phase change behavior compared to small-scale synthesized ones (Fig. 11b). To demonstrate the form stability of large-scale synthesis, samples were exposed to 50 °C for 72 h in an oven and characterized using DSC before and after the heat treatment. Fig. 11c shows that the phase change behavior of PEG ss-PCMs has not been altered. Photos before and after the heat exposure, in Fig. 11d, also illustrate good shape stability of the composite with no footprint of PEG leakage.

4. Conclusion

Driven by our thermal modeling of PCM-integrated walls in buildings, form-stable and fire-safe ss-PCMs with desired practical phase change behavior were developed. Durable TES was experimentally developed, characterized, and validated by producing ss-PCMs when encapsulating optimized mixtures of solid-liquid PEG-based PCMs within synthesized mesoporous MgO supporting material. To achieve its commercial adoption and deployment, maximizing the PCMs' enthalpy change within the operating temperature zone is key to boosting energy efficiency. This is achieved when the PCM has a sharp phase transition peak with both a small temperature glide and a peak melting temperature within the optimum operating temperature range. Targeting commercial deployment, we used National Renewable Energy Laboratory
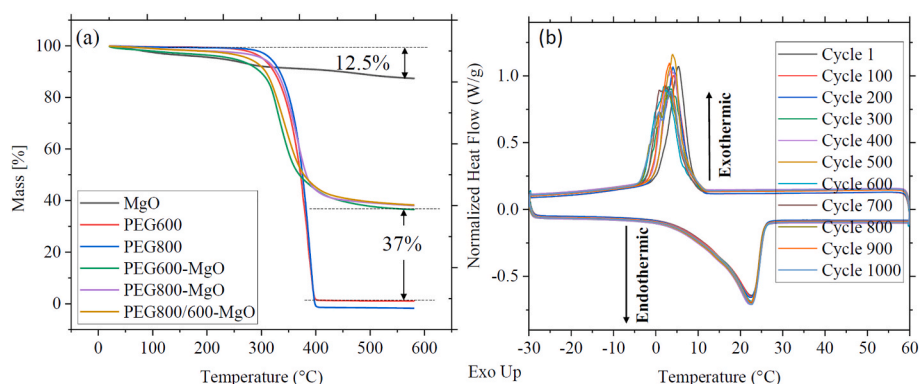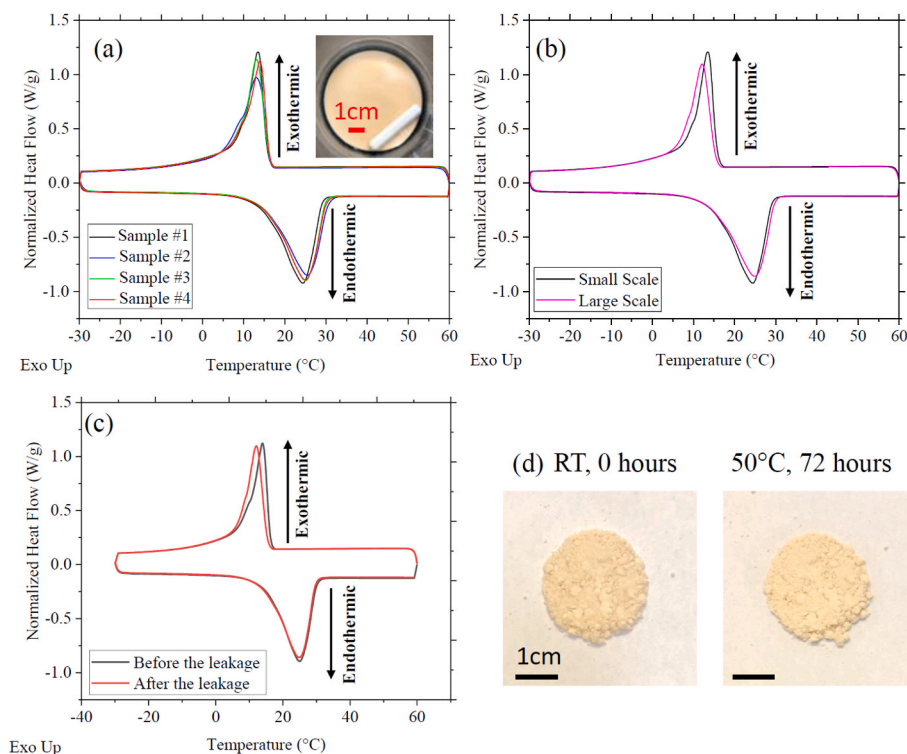

Fig. 10. (a) TGA of MgO, pure PEG, and PEG-MgO ss-PCM; (b) 1000 heating/cooling cycles of PEG PEG800/600 blend (40 wt% 600)-MgO ss-PCM.

Fig. 11. (a) DSC curves of large-scale synthesized PEG800/600 blend-MgO ss-PCM; (b) comparison of phase change behavior of large-scale and small-scale synthesized PEG800/600 blend-MgO ss-PCM; (c) DSC curves; and (d) photos of large-scale synthesized PEG800/600 blend-MgO ss-PCM before and after the leakage test.

(NREL)-developed thermal modeling to guide the experimental material synthesis. We demonstrated the lab-scale synthesis of PEG-MgO ss-PCMs with the desired and optimized phase change behavior. This was achieved by fine-tuning the PEG composition—with different molecular weights—and encapsulating it within synthesized mesoporous MgO. This optimized composition produced a long-term durability composite material—of 1000 phase transition repeatable cycles—with no change in form stability and minimum mass loss. A promising large-scale industrial production method was developed by scaling up the lab-scale synthesis by 100 times.

Our results clearly show how and why the desired phase change behavior improves efficiency under the modeling guidance by quantifying the thermal load shifting of model-driven developed ss-PCMs. The model-driven approach provides guidance on how these ss-PCMs should be tuned for maximized load shifting and ways to bridge the gap between theory and practice when evaluating the energy impact of PCMs. With this approach, we provide a promising and feasible solution for durable and energy-efficient TES composite materials for building applications and beyond. Note that the PCM performance is highly dependent on the indoor and outdoor conditions as well as the building type and application methods. Therefore, developing one PCM that fits all the operating conditions and climates is nearly impossible. However, we strongly believe that the model-guided experimental methods described in this study to develop new PCMs would help future researchers and the building community in this endeavor.

Author contributions

Shuang Cui: Conceptualization, Material synthesis and characterization, Writing-original draft, review, and editing; **Ravi Anant Kishore**: Modeling and simulation, Writing-original draft; **Pranvera Kolari**: Material synthesis and characterization; **Qiye Zheng**: Thermal conductivity measurement; **Sumanjeet Kaur**: Supervision, Writing-Reviewing and Editing, Funding acquisition; **Judith Vidal**: Supervision, Writing-Reviewing and Editing, Funding acquisition; **Roderick Jackson**: Funding acquisition.

Declaration of competing interest

The authors declare that they have no known competing financial interests or personal relationships that could have appeared to influence the work reported in this paper.

Data availability

Data will be made available on request.

Acknowledgement

Appendix A. Supplementary data

Supplementary data to this article can be found online at https://doi.org/10.1016/j.energy.2022.126339.

References

[1] Kalnæs SE, Jelle BP. Phase change materials and products for building applications: a state-of-the-art review and future research opportunities. Energy Build 2015;94: 150–76.

[2] U. S. Energy Information Administration OoEM. Use E. Residential energy consumption survey. 2020.

[3] Khudhair AM, Farid MM. A review on energy conservation in building applications with thermal storage by latent heat using phase change materials. Energy Convers Manag 2004;45(2):263–75.

[4] Song M, et al. Review on building energy performance improvement using phase change materials. Energy Build 2018;158:776–93.

[5] Moreno P, et al. The use of phase change materials in domestic heat pump and air-conditioning systems for short term storage: a review. Renew Sustain Energy Rev 2014;39:1–13.

[6] Guo J, Zhang G. Investigating the performance of the PCM-integrated building envelope on a seasonal basis. J Taiwan Inst Chem Eng 2021;124:91–7.

[7] Wang W, et al. Preparation and performance of form-stable polyethylene glycol/silicon dioxide composites as solid–liquid phase change materials. Appl Energy 2009;86(2):170–4.

[8] Feng L, et al. The shape-stabilized phase change materials composed of polyethylene glycol and various mesoporous matrices (AC, SBA-15 and MCM-41). Sol Energy Mater Sol Cell 2011;95(12):3550–6.

[9] Nurlybekova G, Memon SA, Adilkhanova I. Quantitative evaluation of the thermal and energy performance of the PCM integrated building in the subtropical climate zone for current and future climate scenario. Energy 2021;219:119587.

[10] Zhang Y, et al. Evaluation of paraffin infiltrated in various porous silica matrices as shape-stabilized phase change materials for thermal energy storage. Energy Convers Manag 2018;171:361–70.

[11] Wang C, et al. Shape-stabilized phase change materials based on polyethylene glycol/porous carbon composite: the influence of the pore structure of the carbon materials. Sol Energy Mater Sol Cell 2012;105:21–6.

[12] Min X, et al. Enhanced thermal properties of novel shape-stabilized PEG composite phase change materials with radial mesoporous silica sphere for thermal energy storage. Sci Rep 2015;5:12964.

[13] Li C, et al. Synthesis and characterization of PEG/ZSM-5 composite phase change materials for latent heat storage. Renew Energy 2018;121:45–52.

[14] Sundararajan S, Samui AB, Kulkarni PS. Versatility of polyethylene glycol (PEG) in designing solid–solid phase change materials (PCMs) for thermal management and their application to innovative technologies. J Mater Chem 2017;5(35):18379–96.

[15] Saffari M, et al. Passive cooling of buildings with phase change materials using whole-building energy simulation tools: a review. Renew Sustain Energy Rev 2017; 80:1239–55.

[16] Pasichnyi O, Wallin J, Kordas O. Data-driven building archetypes for urban building energy modelling. Energy 2019;181:360–77.

[17] Wijesuriya S, Brandt M, Tabares-Velasco PC. Parametric analysis of a residential building with phase change material (PCM)-enhanced drywall, precooling, and variable electric rates in a hot and dry climate. Appl Energy 2018;222:497–514.

[18] Wijesuriya S, Tabares-Velasco PC. Empirical validation and comparison of methodologies to simulate micro and macro-encapsulated PCMs in the building envelope. Appl Therm Eng 2021;188:116646.

[19] Saffari M, et al. Economic impact of integrating PCM as passive system in buildings using Fanger comfort model. Energy Build 2016;112:159–72.

[20] Zhao P-P, et al. Nanoflake-constructed supramolecular hierarchical porous microspheres for fire-safety and highly efficient thermal energy storage. ACS Appl Mater Interfaces 2020;12(25):28700–10.

[21] Karaman S, et al. Polyethylene glycol (PEG)/diatomite composite as a novel form-stable phase change material for thermal energy storage. Sol Energy Mater Sol Cell 2011;95(7):1647–53.

[22] Hao Y, et al. Porous MgO material with ultrahigh surface area as the matrix for phase change composite. Thermochim Acta 2015;604:45–51.

[23] Venkata KR, Nagarajan K. Evaluation of heat capacity measurements by temperature-modulated differential scanning calorimetry. J Therm Anal Calorim 2010;102(3):1135–40.

[24] Höhne G, Hemminger WF, Flammersheim H-J. Differential scanning calorimetry. Springer Science & Business Media; 2013.

[25] Rathgeber C, et al. Measurement of enthalpy curves of phase change materials via DSC and T-History: when are both methods needed to estimate the behaviour of the bulk material in applications? Thermochim Acta 2014;596:79–88.

[26] Barreneche C, et al. Study on differential scanning calorimetry analysis with two operation modes and organic and inorganic phase change material (PCM). Thermochim Acta 2013;553:23–6.

[27] Günther E, et al. Enthalpy of phase change materials as a function of temperature: required accuracy and suitable measurement methods. Int J Thermophys 2009;30 (4):1257–69.

[28] McNaughton J, et al. Differential scanning calorimetry. Springer Science & Business Media; 2003.

[29] Kong X, et al. Building energy storage panel based on paraffin/expanded perlite: preparation and thermal performance study. Materials 2016;9(2):70.

[30] Tan B, et al. Preparation and thermal properties of shape-stabilized composite phase change materials based on polyethylene glycol and porous carbon prepared from potato. RSC Adv 2016;6(19):15821–30.

[31] Ma B, et al. Preparation of composite shape-stabilized phase change materials for highway pavements. Construct Build Mater 2013;42:114–21.

[32] Kishore RA, et al. Optimizing PCM-integrated walls for potential energy savings in US Buildings. Energy Build 2020;226:110355.

[33] Kishore RA, et al. Modulating thermal load through lightweight residential building walls using thermal energy storage and controlled precooling strategy. Appl Therm Eng 2020;180:115870.

[34] Kishore RA, et al. Enhancing building energy performance by effectively using phase change material and dynamic insulation in walls. Appl Energy 2021;283: 116306.

[35] Kishore RA, et al. Parametric and sensitivity analysis of a PCM-integrated wall for optimal thermal load modulation in lightweight buildings. Appl Therm Eng 2021; 187:116568.

[36] Bergman TL, et al. Introduction to heat transfer. John Wiley & Sons; 2011.

[37] Biswas K, Abhari R. Low-cost phase change material as an energy storage medium in building envelopes: experimental and numerical analyses. Energy Convers Manag 2014;88:1020–31.

[38] Biswas K, et al. Combined experimental and numerical evaluation of a prototype nano-PCM enhanced wallboard. Appl Energy 2014;131:517–29.

[39] Biswas K, et al. Thermal characterization of full-scale PCM products and numerical simulations, including hysteresis, to evaluate energy impacts in an envelope application. Appl Therm Eng 2018;138:501–12.

[40] Multiphysics C, Module CMHT. COMSOL multiphysics user's guide, vol. 3. COMSOL Multiphysics; 2014. Version.

[41] rredc.nrel.gov, national solar radiation data base. Accessed on July 08, https://rredc.nrel.gov/solar/old_data/nsrdb/1991-2005/tmy3/by_state_and_city.html; 2019.

[42] Web-reference, nside heat balance. Accessed on 06/02, https://bigladdersoftware.com/epx/docs/8-0/engineering-reference/page-021.html; 2021.

[43] American Society of, H., Refrigerating, and E. Air-Conditioning, *Standard method of test for the evaluation of building energy analysis computer programs (ANSI/ASHRAE Addendum b to ANSI/ASHRAE Standard 140-2007)*. American Society of Heating, Refrigerating and Air-Conditioning Engineers; 2010.

[44] Wijesuriya S, et al. Building energy efficiency and load flexibility optimization using phase change materials under futuristic grid scenario. J Clean Prod 2022; 339:130561.

[45] Alkan C, et al. Polyurethanes as solid–solid phase change materials for thermal energy storage. Sol Energy 2012;86(6):1761–9.

[46] Walkenhorst R, Selser J, Piet G. Long-ranged relaxations in poly (ethylene oxide) melts: evidence for network behavior. J Chem Phys 1998;109(24):11043–50.

[47] Choi J, et al. Phase change material-containing mesoporous zeolite composite for adsorption heat recovery. Adv Mater Interfac 2020:2001085.

[48] Alba-Simionesco C, et al. Effects of confinement on freezing and melting. J Phys Condens Matter 2006;18(6):R15.

[49] Schreiber A, Ketelsen I, Findenegg GH. Melting and freezing of water in ordered mesoporous silica materials. Phys Chem Chem Phys 2001;3(7):1185–95.

[50] Pielichowski K, Flejtuch K. Differential scanning calorimetry studies on poly (ethylene glycol) with different molecular weights for thermal energy storage materials. Polym Adv Technol 2002;13(10-12):690–6.

[51] Py X, Olives R, Mauran S. Paraffin/porous-graphite-matrix composite as a high and constant power thermal storage material. Int J Heat Mass Tran 2001;44(14): 2727–37.

[52] Hanif A, Dasgupta S, Nanoti A. Facile synthesis of high-surface-area mesoporous MgO with excellent high-temperature CO2 adsorption potential. Ind Eng Chem Res 2016;55(29):8070–8.

[53] Qian T, et al. The preparation of a green shape-stabilized composite phase change material of polyethylene glycol/SiO2 with enhanced thermal performance based on oil shale ash via temperature-assisted sol–gel method. Sol Energy Mater Sol Cell 2015;132:29–39.

[54] Kohno Y, et al. Photoreduction of carbon dioxide by hydrogen over magnesium oxide. Phys Chem Chem Phys 2001;3(6):1108–13.

[55] Chakraborty S, et al. In vitro & in vivo correlation of release behavior of andrographolide from silica and PEG assisted silica gel matrix. Colloids Surf A Physicochem Eng Asp 2014;455:111–21.

[56] Pan L, et al. Preparation, characterization and thermal properties of micro-encapsulated phase change materials. Sol Energy Mater Sol Cell 2012;98:66–70.

[57] Chen R, et al. Flame-retardancy and thermal properties of a novel phosphorus-modified PCM for thermal energy storage. Chem Eng J 2020;380:122500.

[58] Lai W-C, Chang C-W, Hsueh C-Y. Shape-stabilized poly (ethylene glycol) phase change materials with self-assembled network scaffolds for thermal energy storage. Polymer 2021;213:123196.